Radiation Measurements 187 (2025) 107470

Contents lists available at ScienceDirect

Radiation Measurements

journal homepage: www.elsevier.com/locate/radmeas

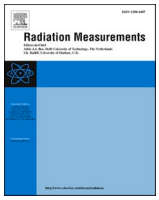

Multiple Coulomb scattering in acrylic of a 221.3 MeV therapeutic proton beam

Skylar Clymer [a], Lukas Domer [a], Arda Gulser [a], Evrim Gulser [a], Ricardo Alarcon [a,*], Paul Mulqueen [b], Stephen Sledge [b], Martin Bues [c]

[a] Department of Physics, Arizona State University, Tempe, AZ, 85287-1504, USA
[b] Proton Calibration Technologies, LLC, Hartselle, AL, 35640, USA
[c] Mayo Clinic Comprehensive Cancer Center, Phoenix, AZ, 85054, USA

ARTICLE INFO

Keywords:
Proton imaging
Thin scintillator
Pellicle mirror
Digital camera
Proton stopping powers
Multiple coulomb scattering

ABSTRACT

Measurements of multiple Coulomb scattering (MCS) distributions for 221.3 MeV therapeutic protons are presented using a novel detector system comprised of a thin scintillator, a pellicle mirror, and a digital camera. The MCS distributions were characterized for three acrylic phantoms of varying lengths and for two biological density-equivalent phantoms simulating bone and muscle. Additionally, beam profiles were measured across an energy range of 80.3–221.3 MeV in 20 MeV increments. The observed energy dependence of the photon yields is consistent with the tabulated stopping power values. The experimental results are benchmarked against Geant4 simulations, demonstrating consistent agreement and validating the capability of the detector system for radiology measurements.

1. Introduction

Proton radiography (PR) and proton computed tomography (PCT) have long been considered advanced alternatives to the conventional use of X-ray CT images for mapping tissue densities in proton therapy (Cormack, 1963; Cormack and Koehler, 1976). In current clinical practice, X-ray CT images are converted into stopping power ratios (SPR) for protons through Hounsfield unit conversions (Raju, 1999; Levi et al., 1982; Schneider et al., 1996), a crucial step for accurately predicting the depth at which proton beams deliver their maximum energy—known as the Bragg peak—within a patient's body (Newhauser and Zhang, 2015; Proton Therapy Physics and Paganetti, 2012). Although this process is standard, it introduces potential errors due to the indirect nature of these conversions. Bragg peak range determined by calibration curves results in uncertainties of 3 %–5 %, depending on tissue inhomogeneities along the proton path. The direct measurement of SPR through proton radiography and PCT holds the potential for highly accurate tissue characterization, reduced radiological dose, and real-time monitoring of the treatment beam, which could improve treatment precision and patient outcomes. Proton-based imaging could further mitigate prediction errors by offering superior density resolution and tissue contrast compared to X-ray CT (Schneider and Pedroni, 1995).

Despite its potential, the clinical adoption of PR and PCT has been constrained by several technical challenges. Chief among these is the complexity of current proton imaging scanners, which are designed to track individual proton histories for image reconstruction (Johnson, 2018). These systems require advanced charged-particle tracking detectors combined with calorimeters, capable of operating at extremely high data rates (>1 MHz). The integration of such intricate systems into modern proton therapy facilities, especially within rotating gantries that must scan over 180° around the patient, poses considerable operational and engineering challenges (Johnson, 2018; Smith et al., 2009). However, notable progress has been achieved in developing proton detection systems tailored for facilities without rotating gantries (Fogazzi et al., 2023; Bashkirov et al., 2016). These systems leverage rotating and translating the patient bed to achieve comparable scanning capabilities, offering a viable alternative in settings where gantry rotation is impractical or unavailable.

When high-energy charged particles traverse a homogeneous material, they undergo a series of small angle scattering processes leading to a final beam distribution characteristic of multiple Coulomb scattering (MCS) (Scott, 1963). Current detector systems used to measure the final proton direction and energy can introduce additional MCS, complicating the reconstruction of proton trajectories—a fundamental requirement in

* Corresponding author.
E-mail address: ralarcon@asu.edu (R. Alarcon).

https://doi.org/10.1016/j.radmeas.2025.107470
Received 23 January 2025; Received in revised form 22 April 2025; Accepted 30 May 2025
Available online 31 May 2025

imaging systems. Advanced trajectory algorithms have been developed to address this, but the complexity remains a significant hurdle (Schulte et al., 2008; Brooke and Penfold, 2020).

In this paper, a novel, simple, and cost-effective detector system is presented that can precisely measure the MCS distribution of protons immediately after their exit from a phantom. This measurement coupled with the known energy and direction of the incoming proton beam can, in principle, be used to reconstruct ideal proton paths. The measured distribution is directly linked to the angular deviation of protons as they pass through a single material, and it can be used to infer the final direction of protons. The standard deviation of the measured MCS distribution is directly linked to the average energy loss by the traversing protons and can be used to infer the proton final energies.

The detector system here introduced consists of a very thin scintillator, placed right after the proton exit point from a phantom, coupled with a pellicle mirror that reflects a fraction of the scintillation light into a commercial digital camera. This setup offers several key advantages: it introduces no additional MCS, it is capable of operating at very high rates, and it can be engineered to function within a rotating gantry environment.

The following sections outline the materials and methods used in this preliminary study (Section 2), present the results of the experimental work and compare them with simulations (Section 3), and conclude with a summary and outlook for future work (Section 4).

2. Materials and methods

2.1. Materials

The following materials were used in the measurements:

- A 1 mm-thick cesium iodide (CsI) scintillator
- A circular pellicle mirror (outside diameter: 88.9 mm; 50/50 transmission-to- reflection ratio)
- A commercial digital camera (Sony A6400)
- Three acrylic phantoms with lengths of 5.1 cm, 10.2 cm, and 15.2 cm, each with a cross-sectional area of 2.54 cm × 2.54 cm.
- Two biological density phantoms, representing bone and muscle, each 5.0 cm in length with cross-sectional areas like the acrylic phantoms.

2.2. Experimental setup

Fig. 1 illustrates the experimental setup at the proton therapy facility at Mayo Clinic, Arizona. The proton beam goes through a thin scintillator producing scintillating light in all directions. The pellicle mirror reflects a fraction of this scintillation back to the digital camera which is positioned to capture the reflected light from the mirror while being shielded from direct radiation exposure along the beam path. The camera could be oriented above, below, or to the side of the scintillator.

The proton therapy facility employs a Hitachi synchrotron (ICSFiles) to accelerate protons to the required energies before delivering them to the target. The CsI scintillator was positioned at the beam's isocenter, with the beam entering from the right. The proton beams were delivered in spot pulses of varying durations–ranging from tens of milliseconds to a few seconds–depending on the prescribed dose. Repetition rates occurred on the order of seconds.

The beam spot size decreased with increasing proton energy due to reduced scattering in the beam nozzle and improve focusing, a critical factor for optimizing treatment plans and ensuring precise dose delivery. Measurements were performed with spots of 4.9 Monitor Units (MU) (Deng et al., 2020) corresponding to approximately 2.2 $\cdot 10^9$ protons. Each spot comprised millisecond pulses delivered at millisecond repetition rates.

2.3. Data acquisition and data reduction

Image acquisition was performed using a digital camera operated via remote control with fixed parameters: 0.1 s shutter speed and ISO 100 sensitivity, yielding an acquisition rate of 2.0 images per second. Each measurement sequence consisted of approximately 40 images, with 50 % attributed to background signal collection. A preliminary selection was performed by calculating the sum of pixel values for each image. An image was included for further analysis if its total pixel sum exceeded

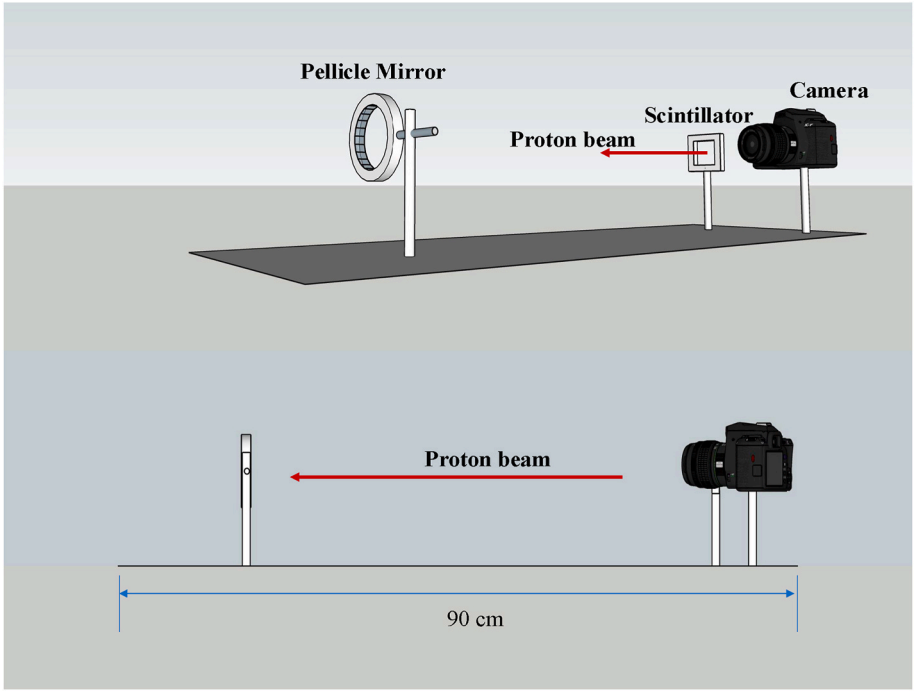

Fig. 1. Experimental Arrangement. The upper panel shows a perspective view of the equipment used and the bottom panel shows a side view of it. Phantoms when used were located directly upstream of the scintillator along the proton beam's path.

the midpoint between the average sums of the five darkest and the five brightest images. No temporal synchronization was implemented between the camera shutter and beam pulse delivery.

The camera's sensor employed a Bayer Filter mosaic architecture to capture wavelength-specific intensity values (red, green, and blue channels). Raw image data were read out using the rawpy Python library to access the Bayer layer information. A median filter was applied to reduce noise, replacing each pixel with the median of its surrounding 3 × 3-pixel neighborhood, and this process was applied across the 4024 × 6048 array.

A uniform flat background subtraction was applied to all selected images. The goodness-of-fit was evaluated using the R^2 correlation coefficient. Each image was then fitted with a Gaussian function using the *curve_fit* function from the SciPy library in Python. By supplying the Gaussian model and the image data, the function estimated the parameters that best matched the data.

2.4. Light capture and energy loss analysis

The pellicle mirror reflected approximately 0.1 % of the isotropic luminescence emitted by high-energy protons passing through the 1 mm thick CsI scintillator. The digital camera captured this reflected light.

The total scintillation yield (S) of CsI is approximately 30,000 photons per MeV of proton energy deposited in the scintillator (Gridin et al., 2014). The relationship between the fluorescent energy emitted per unit path length (dL/dx) and the specific energy loss (dE/dx) for charge particles (in absence of quenching) is (Knoll, 2010):

$$\frac{dL}{dx} = S\frac{dE}{dx} \tag{1}$$

When a proton beam of initial energy E_0 interacts with a thin scintillator, the captured light yield (Y_0) is proportional to the energy loss ΔE_0:

$$Y_0 = \beta S \Delta E_0 \tag{2}$$

Here, β is a geometrical factor that accounts for the fraction of light reflected by the mirror. For protons exiting a target material with energy $E < E_0$, the yield captured Y by the camera can be expressed as:

$$\frac{Y}{Y_0} = \frac{\Delta E}{\Delta E_0} \tag{3}$$

Here, ΔE is the energy deposit in the scintillator by the exiting protons. Equation (3) cancels the geometrical factor β, allowing direct determination of ΔE.

For a 221.3 MeV proton beam, the energy loss in the 1 mm-thick CsI scintillator is $\Delta E_0 = 1.08$ MeV. Measurements were conducted at eight proton energies ranging from 80.3 MeV to 221.3 MeV, corresponding to the expected range of proton exit energies when using the maximum available energy (221.3 MeV).

2.5. Multiple Coulomb scattering (MCS) analysis

A second set of measurements examined the angular distribution of proton beams after traversing various media: acrylic, bone-like, and muscle-like phantoms. Protons exiting the target interacted with the 1 mm CsI scintillator, and the camera recorded the light yield (as defined in Section 2.4). For protons of velocity v traversing a material of length x and radiation length X_0, the root-mean square (RMS) scattering angle θ is given by (Workman et al., 2022):

$$\theta_0 = \frac{13.6\ MeV}{\beta c p}\sqrt{\frac{x}{X_0}}\left[1 + 0.088\log_{10}\left(\frac{x}{\beta^2 X_0}\right)\right], \tag{4}$$

Here, p is the proton momentum and $\beta = v/c$. The experimental MCS standard deviation σ_{exp} results from the convolution (Bromiley, 2014) of the ideal point-beam standard deviation σ_0 and the beam's intrinsic standard deviation σ_b:

$$\sigma_{exp} = \sqrt{\sigma_0^2 + \sigma_b^2} \tag{5}$$

The beam width σ_b was determined from the measurements described in Section 2.4. Analytical predictions from equation (4) and simulations using Geant4 were compared to the measured values of σ_{exp}.

The experimental results were well-modeled by Gaussian distributions representing both the beam profile and MCS effects. Supporting simulations were conducted using the Geant4 software suite, specifically the QGSP_FTFP_BERT physics list, which has been recommended for proton dose calculations (Liu et al., 2022). Results were also compared with the EM_ standard physics list.

The Geant4 simulation models the scattering of a 221.3 MeV proton beam passing through a cubic acrylic prism. The setup includes an acrylic block (5.08 cm × 5.08 cm × L) and a CsI detector (40 mm × 40 mm × 1 mm), all placed within an air-filled world volume (1 m × 1 m × 1 m). The materials used—acrylic, CsI, and air—are represented by Geant4's standard NIST materials: G4_PLEXIGLASS, G4_CESIUM_IODIDE, and G4_AIR, respectively. The CsI detector functions as a sensitive detector, recording the position, energy loss, and deposited energy of any protons that reach it.

The beam is modeled as a monochromatic, unidirectional proton beam incident perpendicularly at the center of the acrylic block. To simulate a realistic beam profile with finite width, the initial transverse positions of the protons are sampled from Gaussian distributions centered at (0, 0)—aligned with the center of the acrylic and the detector—with standard deviations of 2.137 mm, based on the experimental measurements described in Section 3.1. The step size used in each material was the default values calculated by the physics lists (G4EmStandard or QGSP_FTFP_BERT). The maximum step size was varied between 0.1 mm and 1.0 mm with no significant difference in the reported results.

3. Results

3.1. Measurements of therapeutic proton beam profiles

The results corresponding to the methods discussed in Section 2.4 are presented here. Fig. 2 shows the data as detected by the camera sensor for a 221.3 MeV proton beam directly impinging on the scintillator at the beam line iso-center. The left panel displays the image after median filtering (see Section 2.3) and flat background subtraction. The right panel shows the corresponding projection onto one axis, which is fitted with a Gaussian function.

The light yields as a function of the proton beam energy are presented in Fig. 3 (left), alongside a normalized function representing the proton stopping powers obtained from standard tabulations (Stopping-Power, 2024). The photon yields at each energy were determined by summing the pixel values under the 2D beam profile (e.g., Fig. 2 for 221.3 MeV). These sums were corrected for two factors:

1. The energy-dependence of the proton count per Monitor Unit (MU), which is calibrated and specific to the Mayo Clinic facility.
2. Variations in the MU per second (MU/s) delivered during the measurements, as recorded in the beam log.

These corrections allowed estimation of the average proton count per camera frame. The beam energy scan results confirm the assumption that the light captured by the camera accurately represents the proton energy loss in the 1 mm CsI scintillator.

Fig. 3 (right) presents the beam standard deviations as a function of energy, demonstrating improved beam focusing at higher energies. The uncertainties range from 0.8 % to 0.14 %. The beam spot sizes obtained from the 1σ values are consistent with published data from similar facilities (Kraan et al., 2019). Additionally, it is observed that the y-axis

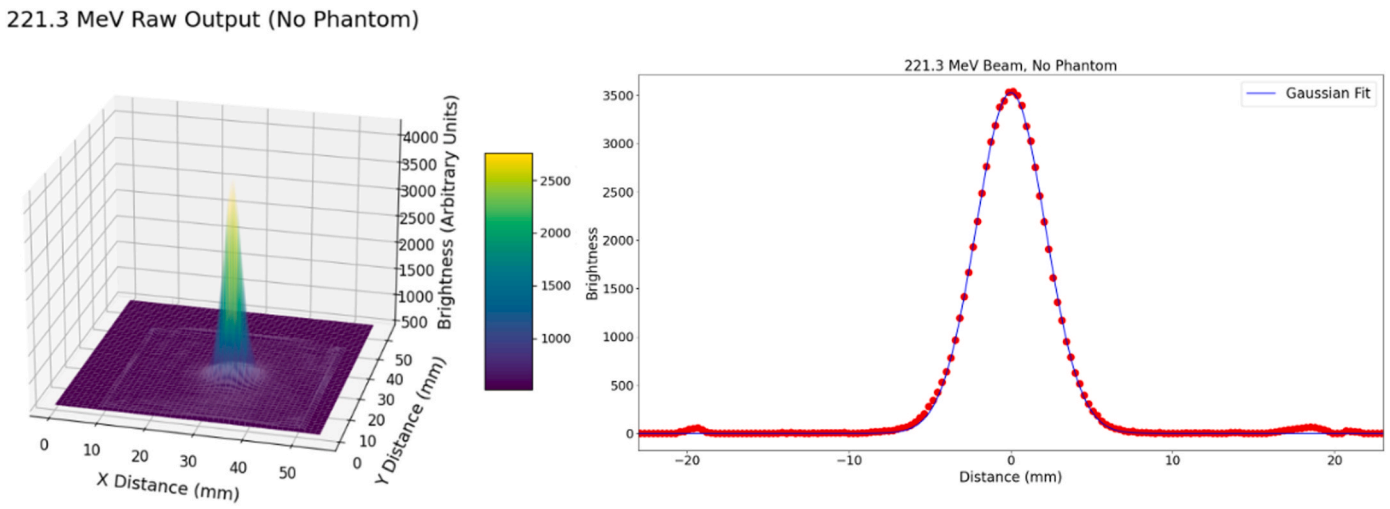

Fig. 2. Beam Profile. Left: the camera sensor pixel distribution. Right: cross-sectional view with a fitted Gaussian.

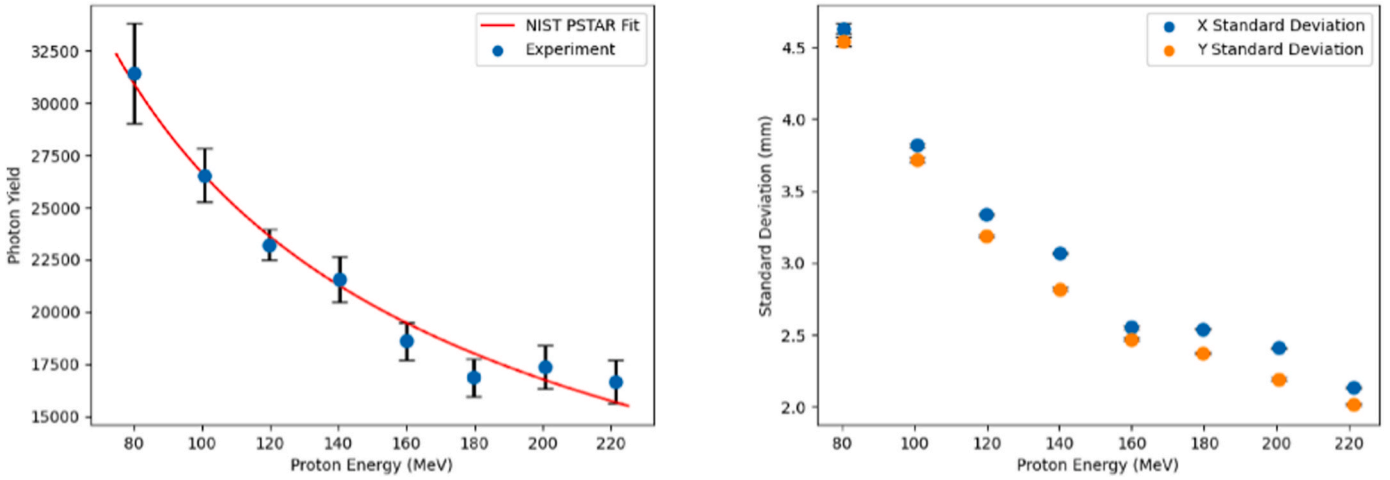

Fig. 3. Beam Energy Scan. Left: average photon yields (arbitrary units) as a function of proton energy fitted with the known stopping powers. The error bars are the 1-sigma uncertainty. Right: the standard deviations (x,y) of the Gaussian functions fitted to the corresponding light yields. The error bars are the 1-sigma standard deviation of the Gaussian fit.

standard deviations are consistently smaller than the corresponding x-axis values.

3.2. Measurements with phantoms

Three acrylic phantoms with lengths of 5.1 cm, 10.2 cm, and 15.2 cm were sequentially placed upstream of the scintillator as close as possible to its position. Each phantom was irradiated with a 221.3 MeV proton beam, with each measurement lasting approximately 1 min of beam time. Fig. 4 shows the measured photon yield distributions for the three acrylic phantoms, fitted with Gaussian functions in the same manner as the beam profiles in Fig. 3.

For comparison, Geant4 simulations were performed, incorporating multiple Coulomb scattering (MCS) as the dominant interaction mechanism for protons in acrylic material. Two cases were simulated:

1. A realistic Gaussian beam with a standard deviation σ_b obtained from the 221.3 MeV beam data (Fig. 2).
2. An ideal point beam at the same energy

The analytical values for σ_o, derived using the multiple scattering angle formula (equation (4)), were compared with the simulation results. Table 1 summarizes the standard deviations for the beam (σ_b), the measured data (σ_{exp}), the extracted point beam distributions (σ_o), and the amplitudes of the experimental MCS distributions.

3.2.1. Discussion of results

Table 1 indicates excellent agreement between the measured and simulated values. This confirms that the point beam distribution (σ_o) can be extracted from measurements made using the Gaussian beam. Both Table 1 and Fig. 4 illustrate that as the phantom thickness increases, the point beam distribution increasingly dominates the measured beam profile.

Fig. 5 plots the standard deviations as a function of phantom length for both measurements and Geant4 predictions. The results highlight the increasing sensitivity of MCS standard deviations in distinguishing between materials of varying densities, such as water, acrylic, and bone.

The standard deviation values also reflect the energy loss of the proton beam as it traverses the material. This is particularly evident in the extracted point beam distributions, as shown in the bottom panel of Fig. 5. Here, the MCS standard deviation tracks the energy loss as the acrylic phantom length increases.

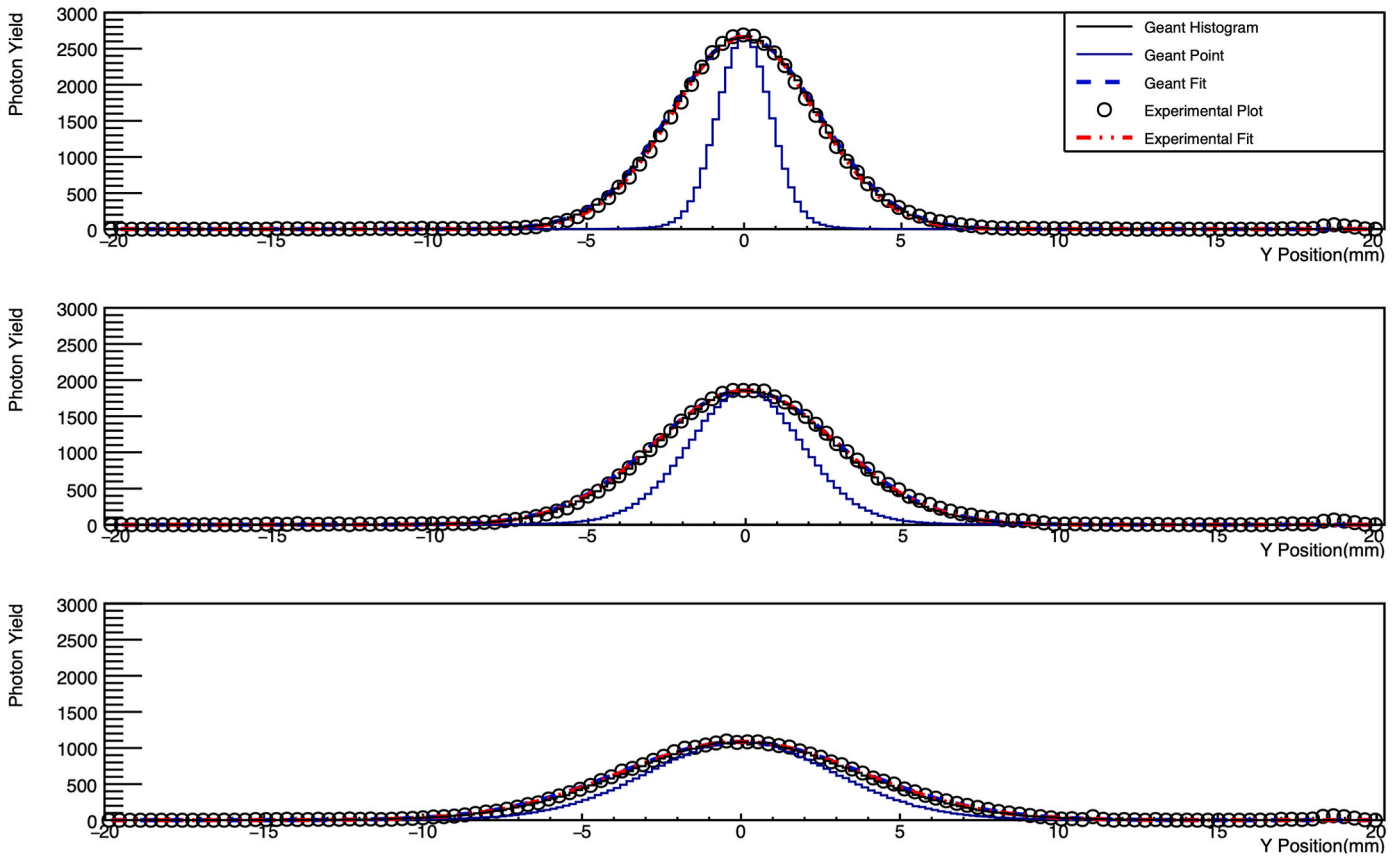

Fig. 4. Multiple Coulomb Scattering (MCS) Distributions for 221.3 MeV protons. Experimental photon yields are shown as open circles (one for every six pixels) from top to bottom for three lengths of the acrylic phantoms (5.1 cm, 10.2 cm, and 15.2 cm). The lines through the points are the fit by a Gaussian (red), and the result of the Geant4 simulation (Geant Histogram) and its Gaussian fit (blue). Also shown (blue histogram) are the MCS distributions obtained in Geant4 using a point beam. (For interpretation of the references to colour in this figure legend, the reader is referred to the Web version of this article.)

Table 1
Parameters of the MCS distributions. The beam σ_b, measured amplitudes and σ_{exp} as a function of the phantom length. The extracted σ_o from the data is compared to the one obtained from Geant4 simulations. The error bars in the standard deviations are the 1-sigma uncertainty whereas the errors in the Amplitudes are 2.576-sigma (99 % confidence level).

E_b (MeV)	L (cm)	σ_b (mm)	Amplitude (counts)	σ_{exp} (mm)	σ_o (data) (mm)	σ_o (Geant4) (mm)
221.3	5.1 (acrylic)	2.137 ± 0.005	2792.3 ± 0.2	2.380 ± 0.004	1.048 ± 0.014	0.961 ± 0.001
221.3	10.2 (acrylic)	2.137 ± 0.005	1839.6 ± 0.3	2.957 ± 0.008	2.044 ± 0.013	1.976 ± 0.002
221.3	15.2 (acrylic)	2.137 ± 0.005	1098.9 ± 0.3	3.849 ± 0.019	3.201 ± 0.023	3.191 ± 0.002
200.4	5.0 (muscle)	2.411 ± 0.003	3237.8 ± 0.3	2.572 ± 0.003	0.660 ± 0.012	0.660 ± 0.001
200.4	5.0 (bone)	2.411 ± 0.003	2811.5 ± 0.4	2.860 ± 0.003	1.235 ± 0.012	1.235 ± 0.001

3.2.2. Energy loss and proton counts

Geant4 simulation results for energy loss and observed proton counts are summarized in Table 2. The table includes the standard deviations, energy loss in acrylic, and proton counts recorded in the scintillator for an initial beam of 200,000 protons. The QGSP_FTFP_BERT results predict a decrease in proton counts as phantom length increases, attributed to non-electromagnetic interactions. This discrepancy cannot be captured with the current detector system, affecting the assumption made in Eq. (3). However, the yields corrected for this loss align well with Geant4 predictions.

Correcting the photon yields for the missing protons, the energy loss in the scintillator was calculated as:

- 1.17 ± 0.13 MeV (5 cm phantom),
- 1.32 ± 0.13 MeV (10 cm phantom), and
- 1.44 ± 0.12 MeV (15 cm phantom).

These values agree closely with the Geant4 predictions in Table 2, validating the approach and confirming the feasibility of using Gaussian beams at the facility for energy loss measurements.

4. Summary

The presented results using the therapeutic proton beams from the Mayo Clinic proton therapy facility in Arizona demonstrate that the proposed detector system can accurately measure the beam profile and the MCS distribution of protons emerging from uniform phantoms of varying lengths. The findings are consistent with Geant4 simulations, providing valuable insights into angular deviation and average energy loss of protons within the medium of interest. These results serve as

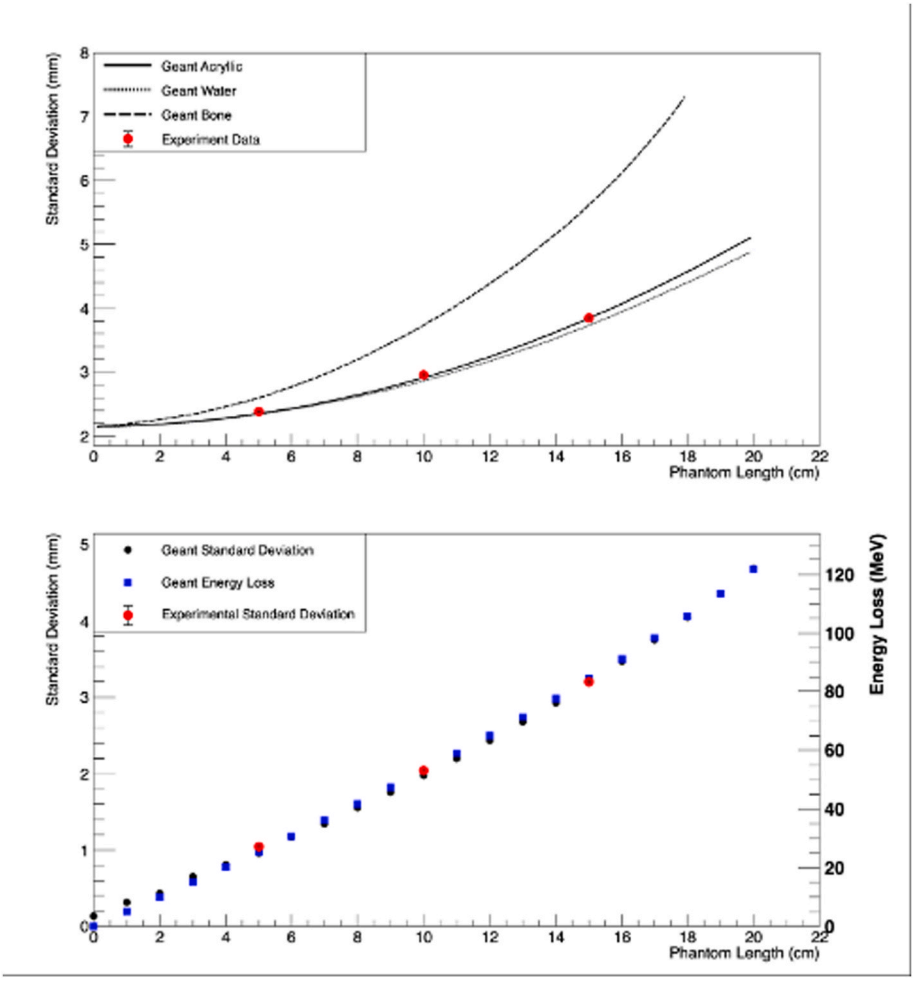

Fig. 5. Acrylic data. Top: The measured standard deviations for the 3 acrylic phantoms as a function of the acrylic length. Geant4 calculations for water, acrylic, and bone are also shown. Bottom: the extracted point beam standard deviation (see Table 1) and the energy loss in the medium of interest as a function of the acrylic length. The size of the experimental points includes the 1-sigma statistical uncertainty.

Table 2
Geant4 comparison results. The acrylic data were simulated for two physics lists in Geant4 and the standard deviations, the extracted energy loss by the beam in the acrylic E^{loss}, and the energy deposit in the scintillator ΔE are listed for the different acrylic lengths. The final number of protons observed is also listed for an entry of 200,000 events in the simulations.

Quantity	EM_Standard	QGSP_FTFP_BERT
$\sigma_{5\ cm}\ (mm)$	2.362 ± 0.004	2.401 ± 0.004
$\sigma_{10\ cm}\ (mm)$	2.949 ± 0.005	2.935 ± 0.006
$\sigma_{15\ cm}\ (mm)$	3.857 ± 0.007	3.845 ± 0.008
$E^{loss}_{5\ cm}\ (MeV)$	25.44 ± 0.91	25.41 ± 1.27
$E^{loss}_{5\ cm}\ (MeV)$	53.10 ± 1.32	53.04 ± 1.55
$E^{loss}_{5\ cm}\ (MeV)$	84.28 ± 1.72	84.20 ± 1.96
$\Delta E_{5\ cm}\ (MeV)$	1.160 ± 0.172	1.200 ± 0.240
$\Delta E_{10\ cm}\ (MeV)$	1.275 ± 0.168	1.295 ± 0.179
$\Delta E_{15\ cm}\ (MeV)$	1.459 ± 0.164	1.470 ± 0.238
Total Counts (5 cm)	199977	188284
Total Counts (10 cm)	199904	174923
Total Counts (15 cm)	199610	160868

proof of principle for a simple and cost-effective detector system.

The measurements were conducted in a short time frame, utilizing the highest delivery of approximately 2.2×10^9 protons per spot, which is impractical for clinical radiation therapy applications. Future steps include significantly reducing the number of protons per spot by at least 2-3 orders of magnitude, a feasible goal with modest modifications to the existing equipment. Enhancements such as faster data acquisition and transfer rates, as well as improved synchronization with proton signals from the accelerator, can further improve photon yield accuracy.

Higher proton energies (>500 MeV) would help mitigate proton loss when traversing substantial material thicknesses. Although the current detector system is not optimized for clinical settings, it holds great promise for use in proton imaging experiments in non-clinical environments.

CRediT authorship contribution statement

Skylar Clymer: Methodology, Formal analysis, Data curation. **Lukas Domer:** Software, Formal analysis. **Arda Gulser:** Software, Formal analysis. **Evrim Gulser:** Software, Methodology, Formal analysis. **Ricardo Alarcon:** Writing – review & editing, Writing – original draft, Supervision, Methodology, Conceptualization. **Paul Mulqueen:** Supervision, Resources, Conceptualization. **Stephen Sledge:** Writing – review & editing, Resources, Methodology. **Martin Bues:** Resources, Investigation.

Declaration of competing interest

The authors declare that they have no known competing financial interests or personal relationships that could have appeared to influence the work reported in this paper.

Acknowledgements

The authors would like to thank Dr. Daniel Robertson (Mayo Clinic) for his help in delivering the therapeutic proton beams used for data collection.

This research did not receive any specific grant from funding agencies in the public, commercial, or not-for-profit sectors.

Data availability

Data will be made available on request.

References

Bashkirov, V.A., Schulte, R.W., Hurley, R.F., Johnson, R.P., Sadrozinski, H.F.-W., Zatserklyaniy, A., Plautz, T., Giacometti, V., 2016. Novel scintillation detector design and performance for proton radiography and computed tomography. Med. Phys. 43 (Issue 2), 664–674.

Bromiley, P.A., 2014. Products and Convolutions of Gaussian Probability Density Functions, Internal Report No. 2003-003, Imaging Sciences Research Group, School of Medicine. University of Manchester.

Brooke, Mark D., Penfold, Scott N., 2020. An inhomogeneous most likely path formalism for proton computed tomography. Phys. Med. 70, 184–195.

Cormack, M., 1963. Representation of a function by its line integrals, with some radiological applications. J. Appl. Phys. 34 (9), 2722–2727.

Cormack, A., Koehler, A., 1976. Quantitative proton tomography: preliminary experiments. Phys. Med. Biol. 21, 560–569.

Deng, W., Younkin, J.E., Souris, K., Huang, S., Augustine, K., Fatyga, M., Ding, X., Collins, M., Bues, M., Shan, J., Stoker, J., Lin, L., Shen, J., Liu, W., 2020. Med. Phys. 47 (6), 2558–2574.

Fogazzi, Elena, et al., 2023. Characterization of the INFN proton CT scanner for cross-calibration of x-ray CT. Phys. Med. Biol. 68, 124001.

Gridin, S., Belsky, A., Moszynski, M., Syntfeld-Kazuch, A., Shiran, N., Gektin, A., 2014. Scintillation properties of CsI: in single crystals. Nucl. Instrum. Methods Phys. Res. A 761, 13–18. https://doi.org/10.1016/j.nima.2014.05.111. ISSN 0168-9002.

https://www.hitachi.com/ICSFiles/afieldfile/2004/06/01/r2003_04_104.pdf.

Johnson, Robert P., 2018. Review of medical radiography and tomography with proton beams. Rep. Prog. Phys. 81, 016701.

Knoll, Glenn F., 2010. Radiation Detection and Measurement, fourth ed. John Wiley & Sons Inc.

Kraan, A.C., Depauw, N., Clasie, B., Madden, T., Kooy, H.M., 2019. Impact of spot size variations on dose in scanned proton beam therapy. Phys. Med. 57, 58–64. https://doi.org/10.1016/j.ejmp.2018.12.011. Epub 2018 Dec 21. PMID: 30738532.

Levi, C., Gray, J.E., McCullough, E.C., Hattery, R.R., 1982. The unreliability of CT numbers as absolute values. AJR Am. J. Roentgenol. 139 (3), 443–447. https://doi.org/10.2214/ajr.139.3.443. PMID: 6981306.

Liu, Buirui, Zhao, Xiandong, Medrano, Maria, 2022. Experimental validation of proton physics models of Geant44 for calculating stopping power ratio. J. Radiol. Prot. 42, 021530.

Newhauser, Wayne D., Zhang, Rui, 2015. The physics of proton therapy. Phys. Med. Biol. 60, R155.

Proton Therapy Physics, 2012. Quality assurance and commissioning. In: Paganetti, Harald (Ed.), Series in Medical Physics and Biomedical Engineering. CRC Press. Chapter 8.

Raju, T.N., 1999. The nobel chronicles. 1979: allan MacLeod Cormack (b 1924); and sir godfrey newbold Hounsfield (b 1919). Lancet 354 (9190), 1653. https://doi.org/10.1016/s0140-6736(05)77147-6. PMID: 10560712.

Schneider, U., Pedroni, E., 1995. Proton radiography as a tool for quality control in proton therapy. Med. Phys. 22 (4), 353–363. https://doi.org/10.1118/1.597470. PMID: 7609715.

Schneider, Uwe, Pedroni, Eros, Lomax, Antony, 1996. The calibration of CT Hounsfield units for radiotherapy treatment planning. Phys. Med. Biol. 41, 111–124.

Schulte, R.W., Penfold, S.N., Tafas, J.T., Schubert, K.E., 2008. A maximum likelihood proton path formalism for application in proton computed tomography. Med. Phys. 35 (11), 4849.

Scott, William T., 1963. Rev. Mod. Phys. 35, 231–314.

Smith, A., Gillin, M., Bues, M., Zhu, X.R., Suzuki, K., Mohan, R., Woo, S., Lee, A., Komaki, R., Cox, J., Hiramoto, K., Akiyama, H., Ishida, T., Sasaki, T., Matsuda, K., The, M.D., 2009. Anderson proton therapy system. Med. Phys. 36 (9), 4068–4083. https://doi.org/10.1118/1.3187229. PMID: 19810479.

Stopping-power & range tables for electrons, protons, and helium ions. NIST Standard Ref. Database 124, 2024. https://www.nist.gov/pml/stopping-power-range-tables-electrons-protons-and-helium-ions.

Workman, R.L., et al., 2022. (Particle data group). Prog. Theor. Exp. Phys. 2022, 083C01 and 2023 update.